Characterization of Deep Convective Cells during the onset of the Indian summer monsoon using C-band polarimetric Doppler Weather Radar observations over Thumba (8.50 N, 770 E)

Venkata Subrahmanyam Kandula[1] and Kishore Kumar Karanam[2]

[1]Space Physics Laboratory VSSC ISRO
[2]Space Physics Laboratory

November 22, 2022

Abstract

The vertical structure and dynamics of deep convective clouds plays an important role during the Indian summer monsoon period. The characteristics of deep convective cells (DCC) and their microphysics remain unclear, especially during the onset phase of the monsoon. Further, the intensity of convection is an important element, which plays a key role in the progression of the monsoon. Thus the present study focuses on characterizing DCC over a coastal location Thumba (8.50 N, 770E) during the onset of the Indian summer monsoon periods of 2017, 2018 and 2019 using C-band polarimetric Doppler Weather Radar (DWR) measurements in terms of their intensity, vertical extent, top heights and their microphysical properties. A method is devised to identify the DCC from the DWR observed reflectivity cross-sections. The results showed that the occurrence of reflectivities in the range of 30-40 dBZ dominates below 6 km and the reflectivities in the range of 10-20 dBZ dominates above 6 km. The diurnal evolution of DCC also been investigated and it is found that these systems peak at three local time intervals viz., 5-7, 11-14 and 16-19 hrs during the study period. The present results provide a quantitative assessment of DCC including their diurnal evolution during the onset of Indian summer monsoon season over Thumba using DWR observations for the first time.

1   **Characterization of Deep Convective Cells during the onset of the Indian summer**

2   **monsoon using C-band polarimetric Doppler Weather Radar observations over**

3   **Thumba (8.5^0 N, 77^0 E)**

4   **Kandula V Subrahmanyam and Karanam Kishore Kumar**

5   Space Physics Laboratory (SPL), Vikram Sarabhai Space Centre (VSSC), ISRO, Trivandrum

6   **E-mail**: kvsm2k@gmail.com

7   **Abstract**

8   The vertical structure and dynamics of deep convective clouds plays an important role during

9   the Indian summer monsoon period. The characteristics of deep convective cells (DCC) and

10   their microphysics remain unclear, especially during the onset phase of the monsoon. Further,

11   the intensity of convection is an important element, which plays a key role in the progression

12   of the monsoon. Thus the present study focuses on characterizing DCC over a coastal

13   location Thumba (8.5^0 N, 77^0 E) during the onset of the Indian summer monsoon periods of

14   2017, 2018 and 2019 using C-band polarimetric Doppler Weather Radar (DWR)

15   measurements in terms of their intensity, vertical extent, top heights and their microphysical

16   properties. A method is devised to identify the DCC from the DWR observed reflectivity

17   cross-sections. The results showed that the occurrence of reflectivities in the range of 30-40

18   dBZ dominates below 6 km and the reflectivities in the range of 10-20 dBZ dominates above

19   6 km. The diurnal evolution of DCC also been investigated and it is found that these systems

20   peak at three local time intervals viz., 5-7, 11-14 and 16-19 hrs during the study period. The

21   present results provide a quantitative assessment of DCC including their diurnal evolution

22   during the onset of Indian summer monsoon season over Thumba using DWR observations

23   for the first time.

24   **Keywords**: Deep Convective Cell (DCC), DWR, Radar reflectivity, Indian summer monsoon

25

1. Introduction

Tropical convective systems play a vital role in general circulation of the atmosphere, rainfall distribution and also in the energy budget of the Earth's atmosphere (Riehl and Malkus, 1958; Tao et al., 2006). Apart from this, the dynamics associated with the convective storms produce severe weather systems and play a crucial role in stratosphere-troposphere exchange processes. The world's deep convection occurs mainly over the tropical belt (e.g., Sherwood and Dessler, 2000; Dessler, 2002; Zipser et al., 2006; Kelley et al., 2010; Xu and Zipser, 2012; Balogun et al., 2020; Wu et al., 2020). These convective cloud systems have a wide range of size, intensity and depth across the globe. Gettelman et al. (2002) studied the distribution of convective clouds and found that the deepest intensive clouds occur over the western Pacific Ocean region. Among many convective systems, the deep convective cells (DCC), whose cloud top extend beyond 12km altitude play a key role in modulating atmospheric dynamics and energetics (e.g., Houze et al., 2015). Recently, Liu and Zipser (2015) examined the deep intense convective storms using one-year Global Precipitation Measurement (GPM) observations and listed the valuable information on these systems. Once the deep convection penetrates into the lower stratosphere and subsequently affects the composition of the stratosphere by pumping water vapour from the troposphere. Therefore, the DCC play a major role in regulating the Earth's climate by transporting heat, water vapour, and momentum from the lower to upper troposphere and lower stratosphere (e.g., Gettelman et al., 2002; Fu et al., 2006; Randel et al., 2010). The DCC is generally associated with intense updrafts, growth of particles in the solid phase and lightning production. Realizing the importance of DCC, there have been numerous studies across the globe to understand its distribution, structure and dynamics. Most of the studies on deep convective systems have been explored by using various space and ground-based measurements such as

microwave and infrared remote sensing measurements from satellite (e.g., Toracinta and Zipser, 2001; Gettelman et al., 2002; Das et al., 2016;), space-based radar and lidar measurements (e.g., Nesbitt et al., 2000, 2006; Cecil et al., 2005; Subrahmanyam and Kumar, 2013; Qie et al., 2014; Liu and Zipser, 2005, 2015; Subrahmanyam and Kumar, 2018; Wu et al., 2020; Subrahmanyam et al., 2020) and ground-based radar (e.g., Cifelli et al., 2002; Kumar et al., 2005; Uma and Rao, 2009).

As aforementioned, the DCC has significant regional characteristics and their microphysical properties also differ from one geographical location to another. Especially, the Indian summer monsoon (ISM) region plays an important role in producing the intense deep convective systems (e.g., Subrahmanyam and Kumar, 2013; Subrahmanyam et al., 2020). There have been many studies on deep convective systems over tropics as well as over the ISM region using space-based observations (e.g., Toracinta and Zipser, 2001; Liu et al., 2003; Liu and Zipser, 2005, 2009; Boccippio et al, 2005; Zipser et al., 2006; Houze et al., 2007; Nesbitt et al., 2010; Schumacher et al., 2010; Romatschke and Houze, 2010, 2013; Romatschke et al., 2010; Houze, 1989; Hence and Houze, 2011; Houze et al., 2015; Subrahmanyam and Kumar, 2013, 2018; Subrahmanyam et al., 2020). Most of the earlier studies focused on the nature of convection using TRMM precipitation radar data and provided new insight into the convective systems. Studies by Hence and Houze (2011& 2012) and Boccippio et al. (2005) documented the statistical behaviour of the vertical structure of convective systems using TRMM radar reflectivity measurements. Though the the space based observations provide information on deep convection across the globe, ground-based radar observations are also equally important to investigate the temporal evolution of the deep convective systems at regional scales. Thus both ground and space based observations of deep convection complement each other. Among ground based

75 observations, DWR provides volumetric measurements of convective systems at high spatial

76 and temporal resolution and able to capture their spatio-temporal evolution at regional scales..

77

78 Even though there are studies on the vertical structure and dynamics of clouds during the

79 Indian summer monsoon period, the characteristics of DCC and their microphysics remain

80 unclear, especially during the onset phase of the monsoon. Further, the intensity of

81 convection is an important element, which plays a key role in the progression of the monsoon

82 (Xu, 2011). To better understand the link between the vertical structure of precipitating

83 clouds and the monsoon progression, it is very important to characterize the vertical structure

84 of DCC embedded in the large-scale monsoon and its evolution. As mentioned earlier, DWR

85 observations of precipitating clouds provide a unique opportunity to characterize the DCC.

86 In this regard, a study is carried out to investigate the distribution of DCC using C-band

87 DWR observations, which is a very first indigenously built polarimetric radar installed in the

88 southern coast of India (Trivandrum, Kerala) to monitor the severe weather systems. In this

89 communication, we present results obtained from C-band DWR observations of spatial and

90 vertical structure of DCC and its diurnal evolution during onset of Indian summer monsoon

91 over Thumba. Section 2 provides the details of the DWR and methodology followed, results

92 are discussed in section 3 and summery is provided in section 4.

93

94 **2. Data and Methodology**

95 C-band DWR operating at Thumba is indigenously developed by Bharat Electronics Limited

96 (BEL) based on technology provided by Indian Space Research Organization (ISRO) in

97 2015. This radar is located in the Indian state of Kerala, which is known as gateway of ISM

98 and is shown in figure1 along with topographical features around the radar site. The radar is

99 located right at coast of the Arabian Sea and flanked by the Western Ghats on the east. C-

band DWR routinely collects a full scan of dual-polarization measurements, which includes the Reflectivity (Z_h), Radial velocity (V) and Spectrum width (σ). The central operating fequency is 5.625 GHz, the peak power is 250 kW, and the gain of the antenna is 45 dB. The more details of the system can be found in Kumar et al. (2020) and Subrahmanyam and Baby (2020). Apart from these base products, polarimetric products such as differential reflectivity factor (Z_{dr}), differential propagation phase (ϕ_{dp}) and cross co-polar correlation coefficient (ρ_{hv}) are also retrieved. Z_{dr} is the ratio, ϕ_{dp} is the phase difference and ρ_{hv} is the correlation between the horizontally and vertically polarized signals. Z_{dr} provides information on the shape and size of the hydrometeors whereas the range derivative of ϕ_{dp} known as specific differential phase (K_{dp}) is very useful in identifying the intense precipitation regions as well as for distinguishing the water droplets from ice. ρ_{hv} is very useful in distinguishing the meteorological and non-meteorological echoes and represents the homogeneity of the radar targets within the radar pulse volume. For the present study, we have used C-band DWR observations over Thumba during the onset phase (1st week of June) of ISM of 2017, 2018 and 2019.
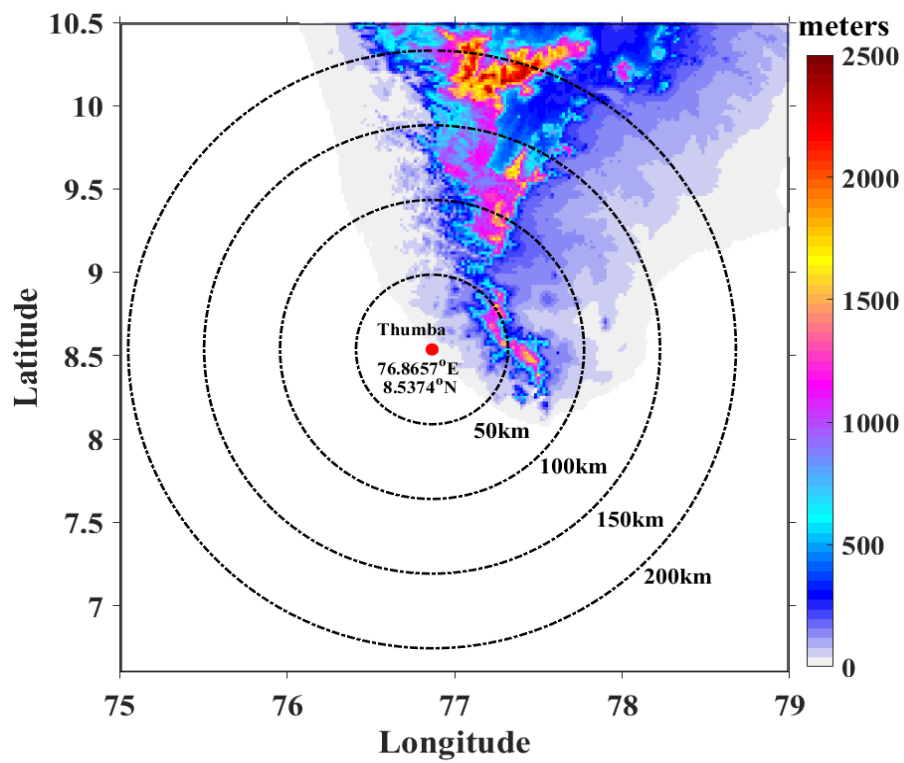
Figure 1: Geographical location of C-band DWR along with topographical features (color map) and radar range circles. The radar location is shown by a red filled circle.
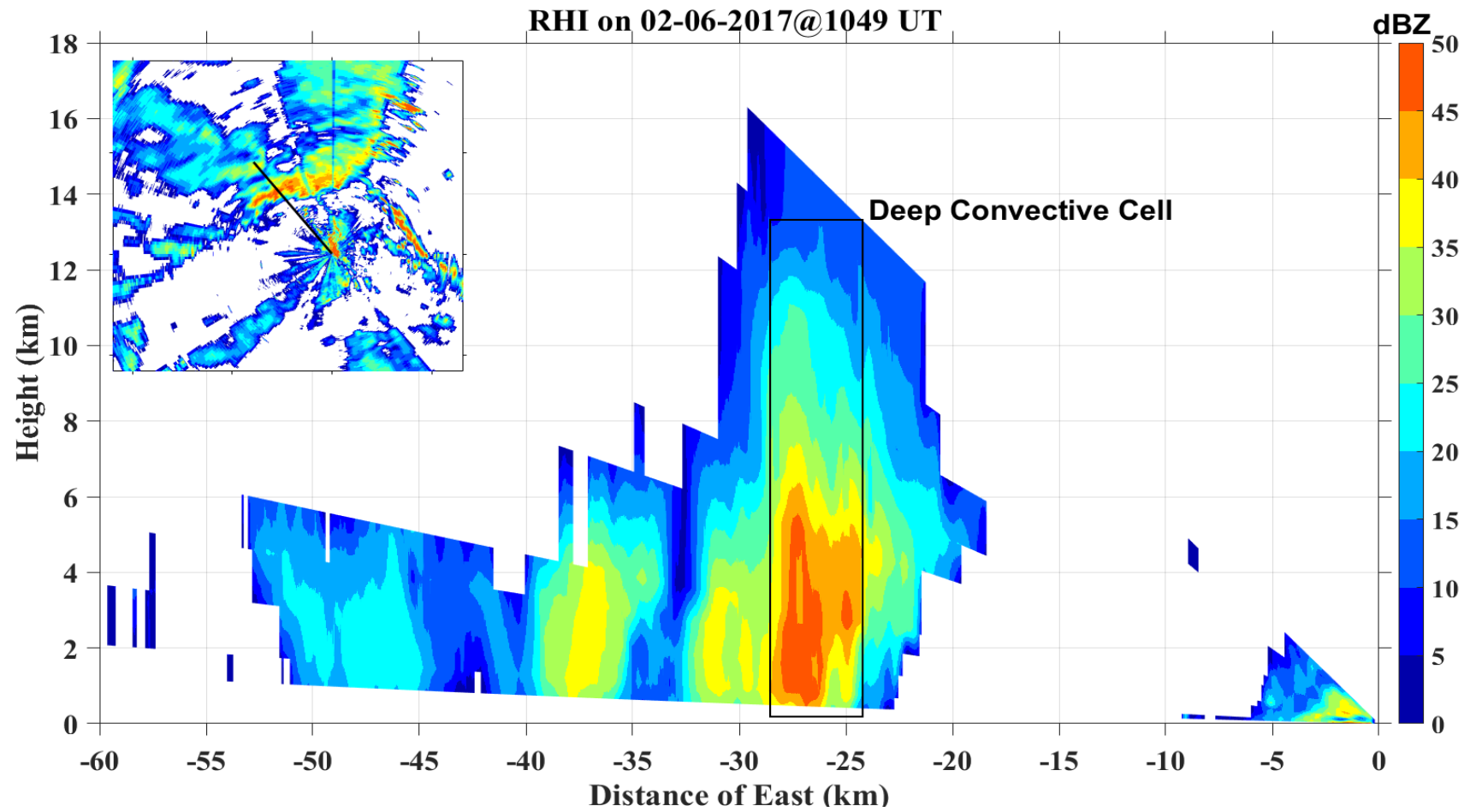
**Figure 2**: A typical range height indicator (RHI) of radar reflectivity corresponding to black solid line shown in the inset.. The cross section shown in the inset depicts the horizontal structure of radar reflectivity at 3 degree elevation on 2nd June at 1049 UT. The rectangular box shown in the figure highlights the DCC.

123   A convective system typically embodies a stratiform and convective element (e.g., Houze,

124   1982) as shown in Figure 2, which depicts a range height indicator of radar reflectivity. The

125   cross section shown in the inset depicts the horizontal structure of radar reflectivity at 3

126   degree elevation on 2nd June 2017 at 1049 UT. The RHI corresponds to the solid black line

127   shown in the inset. The rectangular black box highlights the DCC portion of the convective

128   system, whose echo tops are reaching as high as 14 km. The central objective of the present

129   study is to investigate the number of occurrence of DCC during the onset phase of the ISM.

130   We have followed the widely employed methodology for identifying the DCC profiles from

131   C-band DWR observations (Barnes and Houze, 2013; Zuluaga and Houze, 2013; Houze et

132   al., 2015). The DCC's are defined as those contiguous three dimensional convective C-band

133   DWR echoes exceeding certain thresholds. Figure 3 (a) shows a schematic representation of

134   radar reflectivity profile for identifying the DCC profiles from C-band DWR observations.

135   Figure 3(b) illustrates the flow chart of the present algorithm developed for identifying the

136   DCC. C-band DWR echoes with reflectivity magnitudes ≥40dBZ anywhere in the altitude

137   profile are defined as convective echoes in the first step of identification. Although both 30

138   and 40 dBZ thresholds are better indicators of DCC, we followed 40 dBZ thresholds for

139   stringent DCC identification in the present study (Barnes and Houze, 2013). It is reported that

140   40 dBZ threshold is better suited for identifying the DCC over the land whereas 30 dBZ is

141   better suited over the Oceans (Barnes and Houze, 2013). Further, the identified DCC profiles

142   should have cloud base & top ≤3 km & >10 km, respectively with thickness >6 km as shown

143   in the flow chart. We also estimated the depth of 40 dBZ reflectivity as shown in Figure 3(a).

144   The number of DCC occurrence is estimated as the convective profile counts in each grid

145   point (2 km and 0.5 km intervals in horizontal and vertical). Based on the height coverage,

146   the convective profiles further subdivided into shallow convection, whose cloud tops are

147 below 6 km. Using this methodology, the DCC are identified and their diurnal evolution is

148 also investigated.

149
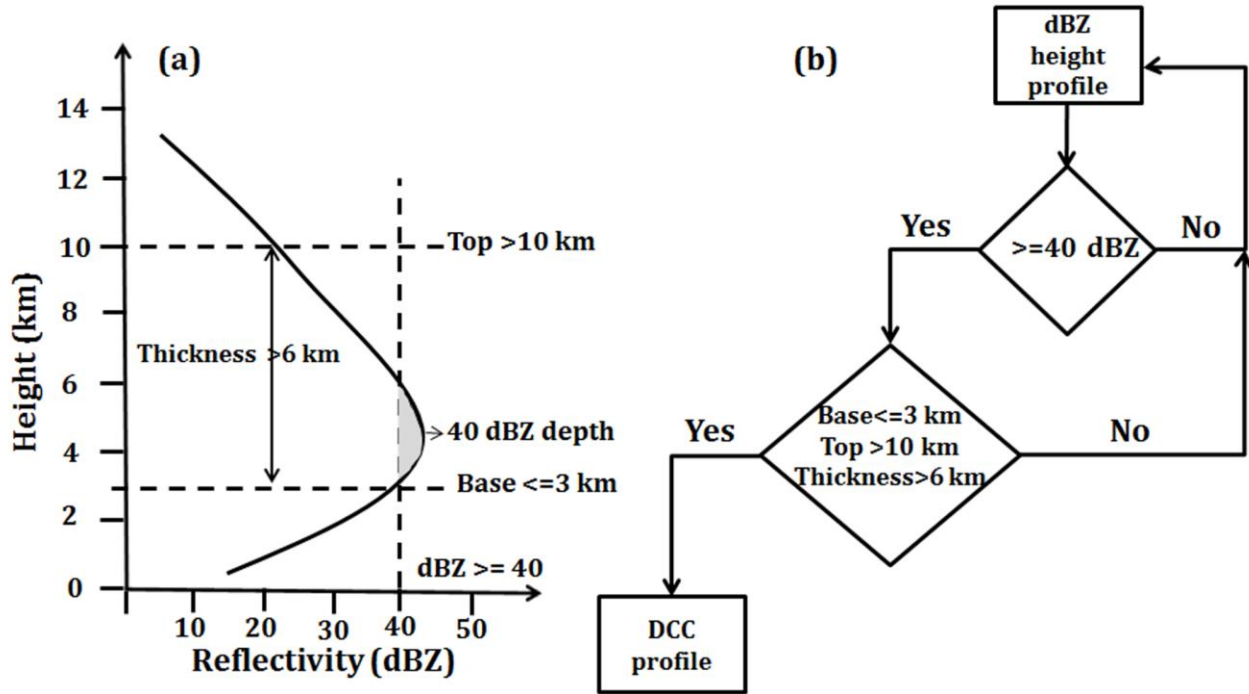
150 **Figure 3**: (a) Schematic representation of radar reflectivity profile for identifying the DCC

151   profiles from C-band DWR observations and (b) Flow chart followed for the DCC

152   identification.

153 **3. Results and Discussions**

154 Figure 4 shows the mean range-height sections of reflectivity and differential reflectivity

155 during the onset of ISM. From this figure, it is evident that the cloud echo tops are extending

156 up to 16 km at ~ 25 km away from the radar location (Figure 4a). The convective core

157 echoes, whose reflectivity values exceed 40 dBZ and above can be seen in figure 4(a) and

158 this type of DCC cores are mainly produced by the young and vigorous convection with

159 strong updrafts (Romastacke et al., 2010). Further, the locations of DCC echoes in the clouds

160 are capable of rapid vertical transport of air from the lower troposphere to the stratosphere as

161 seen in Figure 4(a). It is also known that the impact of convection depends on the depth of the

162 convective cloud (May, 2013). The observed reflectivity at the top of the DCC has the

163 magnitude in 20-25 dBZ range, while the DCC core has reflectivity of the order of 45 dBZ

164 mostly confined between ~3 to 8 km altitude region. There are multiple convective cells

165 embedded within figure 4(a) with horizontal scales extending up to ~100 km. This

166 observation suggests that the observed DCC has the organized convection with multiple cells

167 during the onset of ISM. Homeyer and Kumjian (2015) also observed organized convective

168 systems that contains multiple convective cells using radar measurements. The larger Z_{dr}

169 values are found in the core region of the DCC, as shown in Figure 4(b). These large Z_{dr}

170 values in the convective core region especially above 5 km represent particles coated with

171 super cooled liquid water, which are lifted by the intense updrafts in the DCC. The upper

172 portion of convective core has Z_{dr} values of ~1 dB and corresponding Z_h values are found to

173 be around 20 -25 dBZ . These low-Z_{dr} regions may suggest the presence of nearly isotropic

174 hydrometeors. Figure 4 is an example of a typical system with embedded DCC. The observed

175 reflectivity structure embedded DCC may differ from one case to another. Therefore, to study

176 the generalized structure of DCC, contour frequency by altitude diagram (CFAD) of

177 reflectivity are constructed for the DCC profiles as well as for the shallow convective cases

178 (i.e., radar echo top < 6km) as shown in figure 5. The number of occurrences of reflectivity in

179 each 2 dBZ interval at each 0.5 km height interval is estimated. The number of occurrences at

180 each altitude interval is normalized by the total number of observations at that level following

181 the   method   reported   by   Yutter   and   Houze   (2005).

182

183
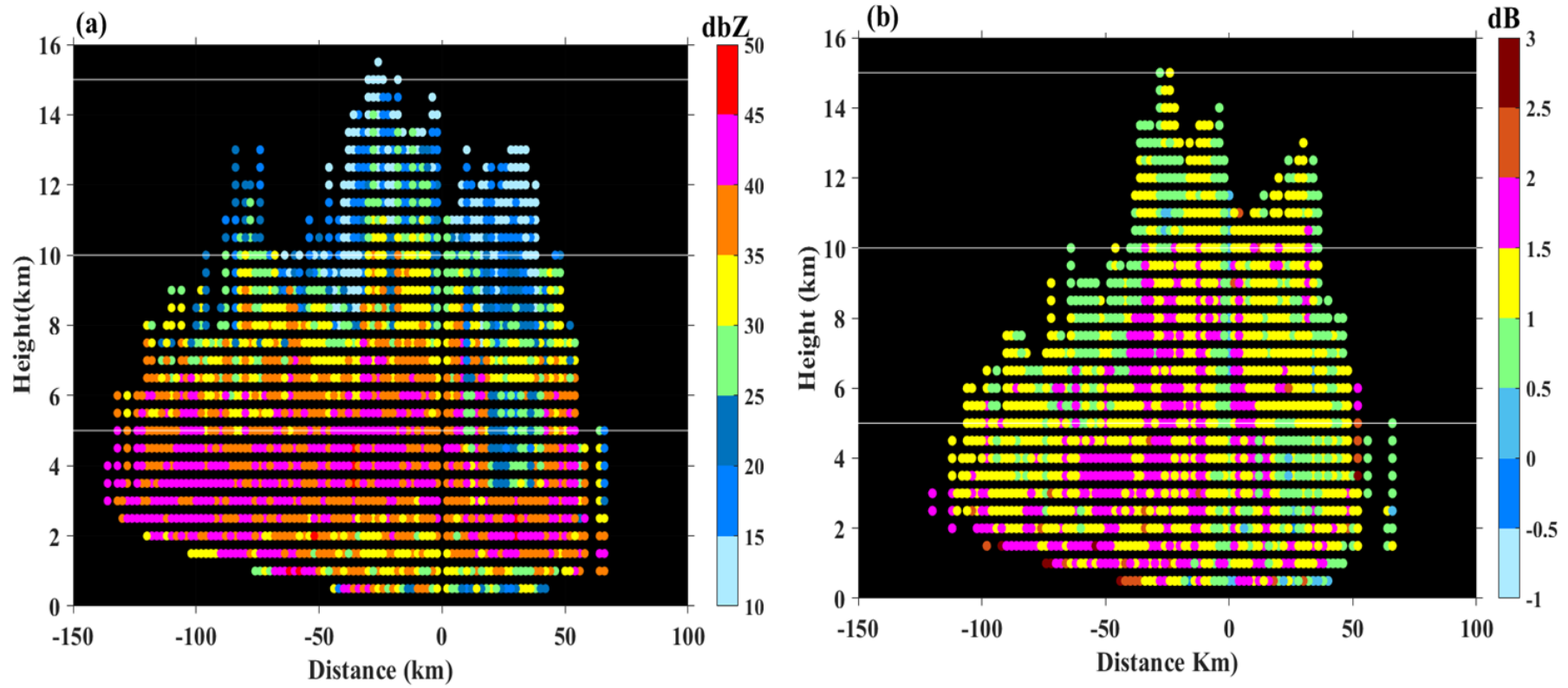
184 **Figure 4**: The mean range-height section of (a) reflectivity and (b) differential reflectivity during the onset of ISM.

3.1 Statistical distribution of Z_h, Z_{dr}, 20 & 40 dBZ echo top height and depth

Figure 5 (a-b) shows the CFAD of Z_h and Z_{dr} for DCC cases and (c-d) for shallow convection cases during the onset of ISM of 2017, 2018 and 2019. The frequency of occurrence of Z_h values in the range of 30 - 40 dBZ dominate the altitude region of 2-6 km and the occurrence of 10-20 dBZ values dominate the altitude region of 7-11 km in the DCC as shown in figure 5(a). The transition of low reflectivity dominant region to relatively high reflectivity dominant region takes place around 5-6 km, which corresponds to 0°C isotherm over the study region. The CFAD depicted in figure 5(a) thus distinguish the liquid water droplet and ice particle region. As mentioned earlier, a typical convective system comprises of convective as well as stratiform region and it is well-known that stratiform region exhibits a large reflectivity around 0°C isotherm in radar observations known as radar bright band. However, in DCC, radar bright band will be absent due to intense up and down drafts. Intense outliers occur at all the altitude levels below 6-7 km in DCCs with Z_h as high as 40 dBZ and above. The range of reflectivity distribution narrows down from lower to upper troposphere. As the monsoon convection has the maritime characteristics with less electrical nature, there can be a rapid decrease of Z_h above the freezing altitude as seen in Figure 5(a) along with the presence of graupel or hail (Keenan and Carbone 1992; May and Ballinger, 2007). There is a substantial population of ~ 30 dBZ reflectivity in the DCC with tops exceeding ~12 km. The echo tops reaching as high as 14-15 km confirms that the observed profiles are associated with the DCC. Most of the earlier studies using space based radar observations reported the vertical structure of precipitating clouds over the Western Ghats during the ISM having echo tops reaching ~10 km. The present analysis on the other hand shows DCC reaching as high as 14 km during the onset of the ISM as depicted in figure 5(a). Due to limited temporal sampling of the space based radars, there is a chance that these systems might have under sampled the DCC. The distribution of Z_h at high altitudes shows
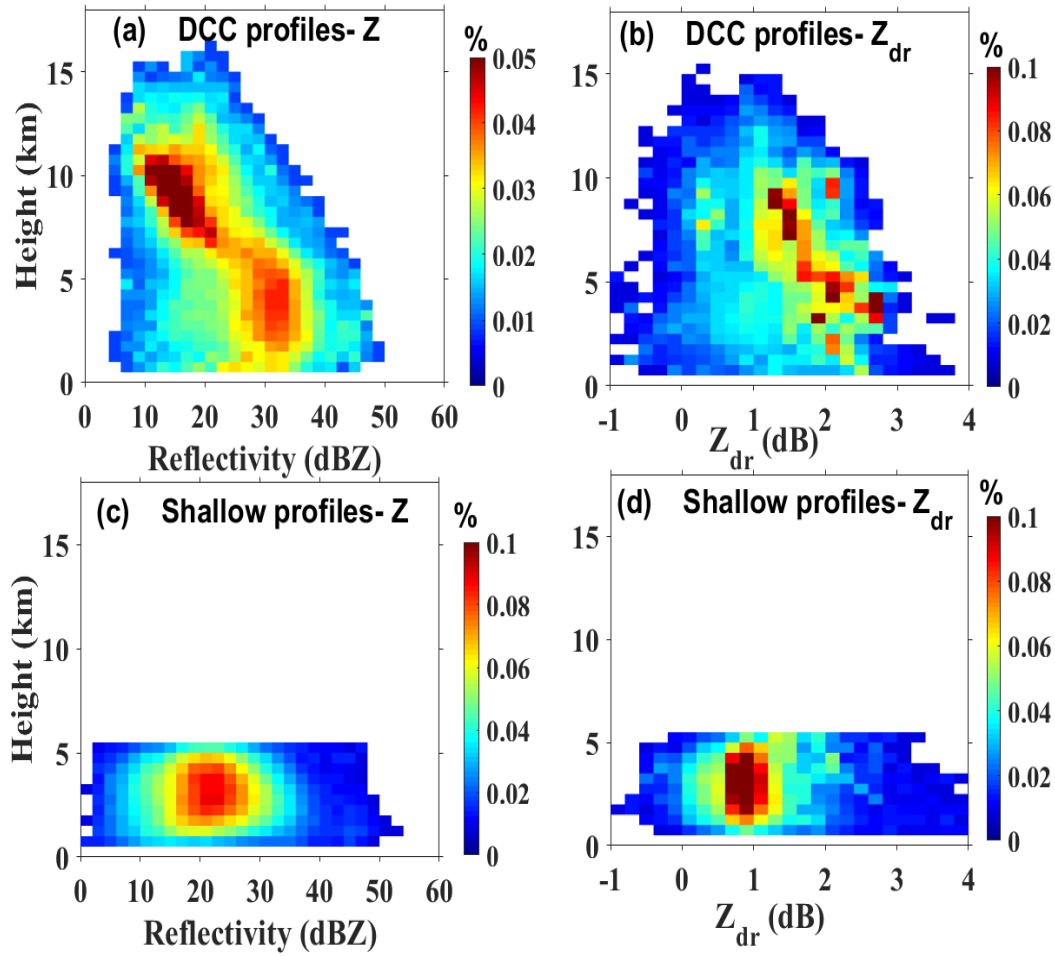
Figure 5: Contour Frequency Altitude Distribution (CFAD) of C-band DWR measured (a) Radar reflectivity and (b) Differential Reflectivity for the DCC. The CFADs shown in (c) and (d) are same as (a) and (b), respectively but for the shallow convection cases. The C-DWR observations during the onset of ISM of 2017, 2018 and 2019 are used to construct the CFADs,

the low frequency of occurrence of relatively high Z_h values of the order of 30-40 dBZ indicating the presence of graupel or small hail. The vertical velocities in the deep convective core are several meters per second or greater (e.g., Kumar et al., 2005). This is one of the principal reasons for the higher cloud tops in the DCC exceeding above ~14 km. In the presence of such strong updrafts, the dominant growth mechanism for precipitation particles is the collection of cloud water by the larger drops and/or ice particles sweeping out the cloud

222   water in their fall paths (e.g., Kirankumar et al., 2008). Moreover, the strong updrafts allow

223   for the larger particles to grow for a long period. These updrafts of the growing particles

224   increase their residence time in the cloud and thus their opportunities to form as bigger

225   hydrometeors as seen in Figure 5(b). This figure depicts the CFAD of Z_{dr} corresponding to

226   the radar reflectivity shown in figure 5(a). From this figure, it is evident that the larger Z_{dr}

227   values (~ 2- 3 dB) representing large droplets are confined in the 1- 10 km altitude region.

228   These larger Z_{dr} values further suggest that the DCC core region has the stronger updrafts,

229   which facilitate the formation of larger diameter droplets as discussed earlier. The smaller Z_{dr}

230   values (~ 1 dB or less) are found above 10 km altitude, which indicates that those regions are

231   dominated by nearly isotropic hydrometeors. Figure 5(c) shows the CFAD distribution of Z_{h}

232   in shallow convective clouds during onset of ISM. The frequency of occurrence peaks at ~22

233   dBZ in the ~ 1.5 to 4 km altitude region. In shallow convective cases, the maximum Z_{h} value

234   is found to be around ~ 50 dBZ, whereas the maximum concentration of Z_{dr} found to be

235   around 1 dB as seen from Figure 5(c & d). These observations are consistent with the warm

236   rain processes, which is one of the dominant modes of precipitation during ISM. Thus figure

237   5 summarizes the observed features of the DCC in terms of frequency of occurrence of radar

238   reflectivity and differential reflectivity.

239

240   This section focuses on the spatial distribution of 20 and 40 dBZ echo top heights in the DCC

241   during the onset of ISM. In general, 20 dBZ echo top is a reasonable reflectivity threshold of

242   the storm activity (e.g., Wu et al., 2018). In this study, we have also considered 40 dBZ echo

243   top height, which indicates the intense convection (e.g., Goudenhoofdt and Delobbe, 2013).

244   Figure 6 shows the spatial distribution of mean 20 and 40 dBZ echo top heights in the DCC.

245   The maximum occurrences of 20 dBZ echo top height is found to be around 7-9 km altitude

246   and concentrated within 50 km radius from radar center during the onset of ISM. There are a

247 few regions, where 20 dBZ echo top height exceeds beyond 10 km in the DCC. In fact, this

248 aspect can be inferred from figure 5(a) itself; however, figure 6(a) provides the spatial

249 distribution of 20 dBZ top heights. On the other hand, the echo tops of 40 dBZ, which are

250 associated with very intense convection, are having mean heights of 2-3 km and exceeding 4

251 km on a few occasions as shown in Figure 6 (b). Romatchke and Houze (2011) observed that

252 mean reflectivity of 40 dBZ echo tops are reaching up to 6 km in deeper convective systems

253 during South Asian monsoon using TRMM observations. Zhang et al. (2006) also observed

254 that the deep convective systems have echo tops between 6 and 12 km over China. The

255 regions with relatively high 40 dBZ echo tops play an important role in producing the large

256 precipitation and occasionally penetrate into the lower stratosphere. The locations of 40 dBZ

257 radar echoes also indicate the lightening regimes (Xu and Zipser, 2012; Liu et al., 2012).

258 Further, we estimated the depth of 40 dBZ echoes as discussed in section 2. Figure 6(c)

259 shows the spatial distribution of 40 dBZ echo depths in the DCCs. This quantity indicates the

260 depth of strong convection in the DCC during the onset of ISM. The maximum depth of 40

261 dBZ echoes is found to be around 4 km with fewer occurrences and the depths in the range of

262 1.5 - 2 .5 km has maximum occurrences. From this figure, it can be inferred that the storm top

263 heights can reach as high as 14 km occasionally with intense convection up to 6 km with a

264 maximum depth of 4 km during the onset of ISM. One more inference that can be drawn

265 from figure 6 is that there is a preferential formation of DCC with higher echo top heights

266 and depth over oceanic region as compared to land region during the initial phase of the
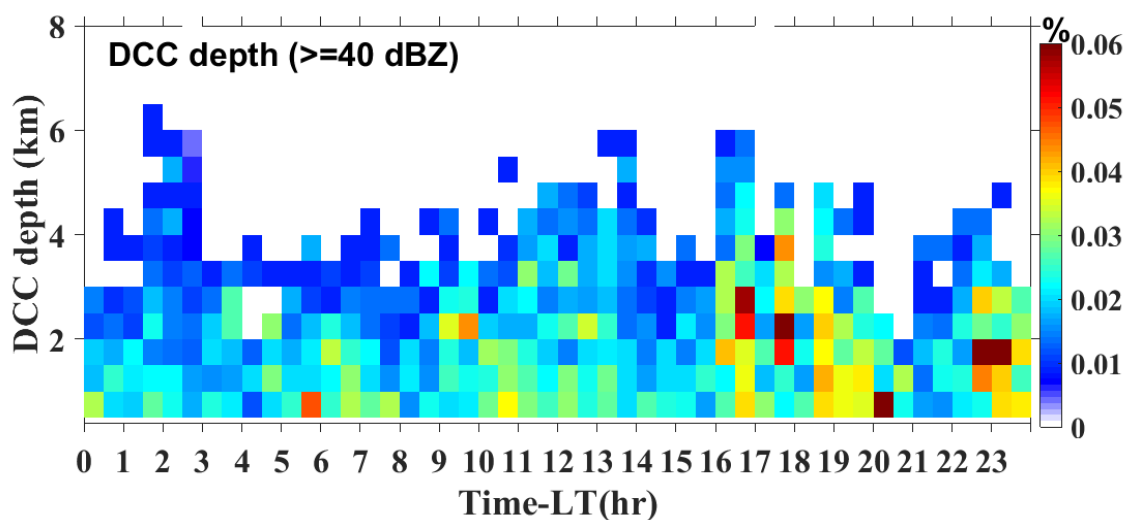
267 monsoon.

268

269

270
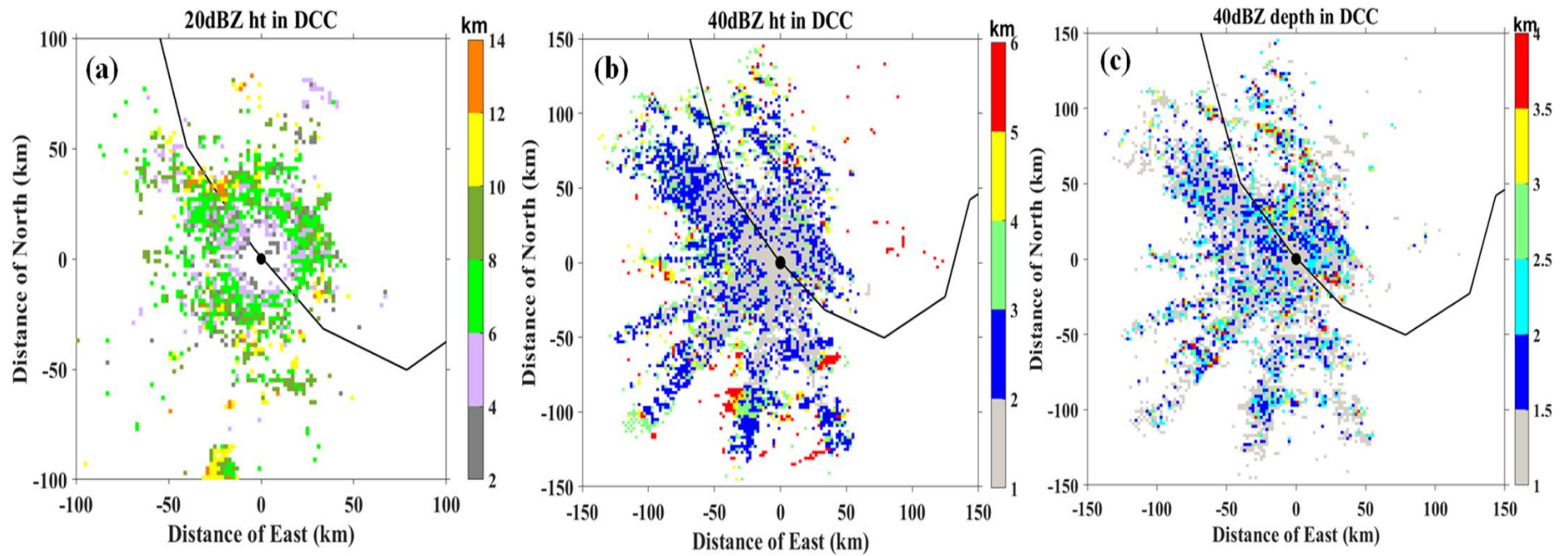
Figure 6: Spatial distribution of (a) 20, (b) 40 dBZ mean echo top heights and (c) 40 dBZ echo depth in the DCC observed during the onset phase of ISM of 2017, 2018 and 2019.

273

274

275   Figure 7(a) shows the mean vertical profile of 20 (dotted line) and 40 dBZ (solid line) radar

276   echo precipitation features and 7(b) shows the 40 dBZ radar echo depth in the DCC. The

277   maximum occurrence of 40 dBZ is found to be 30% at about 2km altitude level and a

278   secondary peak of occurrence is found to be between 4 to 6 km altitude levels. In contrast to

279   40 dBZ radar echoes, the maximum occurrence of 20 dBZ is found to be around 7 km level.

280   The maximum occurrence of depth of 40 dBZ echoes is found to be below 3km level (Figure

281   7b). Therefore, 20 and 40 dBZ radar echoes in the DCCs peaks in upper and lower

282   tropospheric altitudes, respectively. These profiles represent the mean characteristics of the

283   vertical extent of the DCC with information on the intense part of these systems. As the

284   secondary peaks of 40 dBZ in the upper level and 20 dBZ in lower levels may be associated

285   with the isolated convective systems, which are typically small in horizontal scales.

286
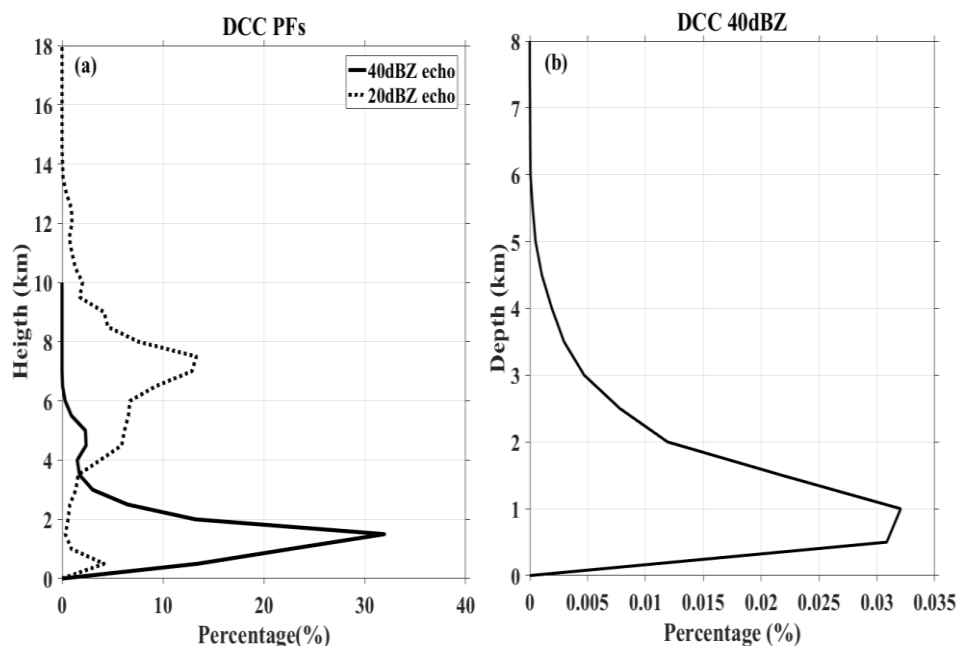
288   **Figure 7**: Vertical profile of frequency of occurrence of 20 and 40 dBZ mean echo top

289   heights in the DCC.

290

291

292   Figure 8 shows the diurnal evolution of occurrence of 40 dBZ reflectivity as a function of

293   echo depth. As mentioned earlier, the depth of 40 dBZ reflectivity represent the intense

294   convective systems. From this figure, it is evident that the 40 dBZ reflectivity occurance

295   peak at three local time intervals viz., 5-7, 11-14 and 16-19 hrs LT with varying depths

296   during the study period. Apart from these, a mid-night peak is also observed. The maximum

297   occurrences of DCC at these local times are associated with depths below 4 km as seen in

298   Figure 8. In general, the convective systems with echo tops above 7 km are having relatively

299   smaller area during early morning and midnight, while they are relatively larger in area

300   during late-evening and night times. Homeyer and Kumijan (2015) also observed that the

301   convective storms are typically small in spatial scales in late-afternoon and further evolve

302   into organized convective systems that persist overnight.

303

304

305   **Figure 8**: Diurnal evolution of 40 dBZ depth observed by C-band DWR during the study

306   period.

4. Summary

The present study characterized the spatial distribution of the DCC by employing the C-band DWR observations during the onset of the ISM of 2017, 2018 and 2019. The important results are summarized below.

1. A method similar to Barnes and Houze (2013) is devised to identify the DCC profiles in volumetric C-band DWR observations, based on this method an algorithm is devised to estimate frequency of occurrence of DCC during the study period.

2. The frequency of occurrence of DCC is quantified using CFAD. The echo tops are noted to be reaching as high as 14-15 km, which were not noted in the earlier spaced based observations. It is also noted that the distribution of Z_h narrows down from lower to upper troposphere. The occurrence of reflectivities in the range of 30-40 dBZ dominates below 6 km and the reflectivities in the range of 10-20 dBZ dominates above 6 km. A marked shift is noted at 5-6 km in the CFAD.

3. Larger (smaller) Z_{dr} values are found below (above) 10 km in DCC regions. However, the observed Z_{dr} values at higher altitude above 10 km are relatively low, which may be attributed to isotropic nature of hydrometeors at these altitudes. Larger values of Z_{dr} are observed less frequently at higher altitudes and this may be attributed to the presence of graupel or small hail.

4. The CFAD for shallow convective systems are also constructed, which show the dominance of 20-30 dBZ occurrence and nearly isotropic hydrometeors during the study period.

5. The statistical distribution of 20 and 40 dBZ echo top heights and depths in DCC are estimated. The threshold of 20 dBZ is used to find the DCC boundaries whereas 40 dBZ thresholds are used to find the intense part of the DCC.

331   6. The maximum depth of 40 dBZ echoes is found to be around 4 km with fewer

332   occurrences and a depth of 2 km having maximum occurrences.

333   7. The diurnal evolution of DCC is also investigated in terms of frequency of occurrence

334   of 40 dBZ echo depth and found that it peaks at three local time intervals viz., 5-7, 11-

335   14 and 16-19 hrs LT during the onset of the ISM.

336 The present study thus brought out the observed features of DCC during the onset of the ISM.

337 It is known that the latent heat released in the DCC are one of the important drivers of the

338 monsoon circulation and the results discussed in the present study may be helpful to

339 delineating the role of DCC formed during the onset in the progression of the ISM.

340 **Acknowledgments**

344

345 **References**

346 Balogun, R.A., et al. (2020), Vertical structure and frequencies of deep convection

347   during active periods of the West and Central African monsoon season, Theor. Appl.

348   Climato., https://doi.org/10.1007/s00704-020-03203-6.

349 Barnes, H. C., and R. A. Houze Jr. (2013), The precipitating cloud population of the

350   Madden-Julian Oscillation over the Indian and West Pacific Oceans, J. Geophys. Res.

351   Atmos., 118, 6996– 7023, doi:10.1002/jgrd.50375

352 Boccippio, D. J., W. A. Petersen, and D. J. Cecil (2005), The tropical convective spectrum.

353   Part I: Archetypal vertical structures, J. Clim., 18, 2744– 2769.

354 Cifelli, E., W. A. Peterson, L. D. Carey, S. A. Rutledge, and M. A. F. Silva Dias (2002),

355   Radar observations of the kinematic, microphysical, and precipitation characteristics

356   of two MCSs in TRMM LBA, J. Geophys. Res., 107, 8077.

357 Davies, L., C. Jakob, P. May, V. V. Kumar, and S. Xie (2013), Relationships between the

358   large-scale atmosphere and the small-scale convective state for Darwin, Australia, J.

359   Geophys. Res., 118, 11,534–11,545, https://doi.org/10.1002/jgrd.50645.

360 Dessler, A. E. (2002), The effect of deep, tropical convection on the tropical tropopause

361   layer, J. Geophys. Res., 107 (D3), 4033, DOI: 10.1029/2001JD000511, 2002.

362 Fu, R., et al. (2006), Short circuit of water vapor and polluted air to the global stratosphere

363   by convective transport over the Tibetan Plateau, Proc. Natl. Acad. Sci. U. S. A., 103,

364   5664–5669.

365 Gettelman, A., M. L. Salby, and F. Sassi (2002), Distribution and influence of convection in

366   the tropical tropopause region, J. Geophys. Res., 107 (D10).

367 Goudenhoofdt, E. and L. Delobbe (2013), Statistical Characteristics of Convective Storms in

368   Belgium Derived from Volumetric Weather Radar Observations, J. Appl. Meterol.

369   Climatol., 52, 918-934, 2013

370 Hence, D. A., and R. A. Houze Jr. (2011), Vertical structure of hurricane eyewalls as seen by

371   the TRMM Precipitation Radar, J. Atmos. Sci., 68, 1637– 1652.

372 Hence, D. A., and R. A. **Houze**, Jr. (2012), Vertical structure of tropical cyclone rainbands as

373   seen by the TRMM Precipitation Radar, J. Atmos. Sci., **69**, 2644–2661.

374 Homeyer, C.R. and M.R. Kumjian (2015), Microphysical Characteristics of Overshooting

375   Convection from Polarimetric Radar Observations, J. Atmos. Sci., 72, 870-891.

376 Houze, R. A., Jr. (1982), Cloud clusters and large-scale vertical motions in the tropics, J.
377   Meteorol. Soc. Jpn., 60, 396– 410.

378 Houze, R. A., Jr. (1989), Observed structure of mesoscale convective systems and
379   implications for large-scale heating, Q. J. R. Meteorol. Soc., 115, 425– 461.

380 Houze, R. A., Jr. (2004), Mesoscale convective systems, Rev. Geophys., 42, RG4003,
381   doi:10.1029/2004RG000150.

382 Houze, R. A., Jr., and D. D. Churchill (1987), Mesoscale organization and cloud
383   microphysics in a Bay of Bengal depression, J. Atmos. Sci., 44, 1845– 1868.

384 Houze, R. A., Jr., D. C. Wilton, and B. F. Smull (2007), Monsoon convection in the
385   Himalayan region as seen by the TRMM Precipitation Radar, Q. J. R. Meteorol. Soc.,
386   133, 1389– 1411.

387 Houze, R. A., Jr., K. L. Rasmussen, M. D. Zuluaga, and S. R. Brodzik (2015), The variable
388   nature of convection in the tropics and subtropics: A legacy of 16 years of the
389   Tropical Rainfall Measuring Mission (TRMM) satellite, Rev. Geophys., **53**,
390   doi:10.1002/2015RG000488.

391 Keenan, T. D., and R. E. Carbone (1992), A preliminary morphology of precipitation systems
392   in tropical northern Australia, Quart. J. Roy. Meteor. Soc., 118, 283–326.

393 Kelley, O. A., J. Stout, M. Summers, and E. J. Zipser (2010), Do the tallest convective cells
394   over the tropical ocean have slow updrafts?, Mon. Weather Rev., 138, 1651–1672,
395   doi:10.1175/2009MWR3030.1.

396 Kirankumar, N. V. P., T. N. Rao, B. Radhakrishna, and D. N. Rao (2008), Statistical
397   characteristics of raindrop size distribution in southwest monsoon season, J. Appl.
398   Meteorol. Climatol., 47, 576–590.

399 Konwar, M., S. K. Das, S. M. Deshpande, K. Chakravarty, and B. N. Goswami (2014),

400   Microphysics of clouds and rain over the Western Ghat, J. Geophys. Res. Atmos.,

401   119, 6140–6159, doi:10.1002/ 2014JD021606.

402 Kumar, S., A. Hazra, and B. N. Goswami (2013), Role of interaction between dynamics,

403   thermodynamics and cloud microphysics on summer monsoon precipitating clouds

404   over the Myanmar Coast and the Western Ghats, Clim. Dyn., 1–14,

405   doi:10.1007/s00382-013-1909-3.

406 Kumar, K. K., A. R. Jain, and D. N. Rao (2005), VHF/UHF radar observations of tropical

407   mesoscale convective systems over southern India, Ann. Geophysicae, 23, 1673–

408   1683.

409 Liu, C. (2011), Rainfall contribution from precipitation systems with different sizes,

410   intensities and durations, J. Hydrometeorol., 12, 394– 412.

411 Liu, C., and E. J. Zipser (2005), Global distribution of convection penetrating the tropical

412   tropopause, J. Geophys. Res., 110, D23104.

413 Liu, C., and E. J. Zipser (2009), "Warm rain" in the tropics: Seasonal and regional

414   distribution based on 9 years of TRMM data, J. Clim., 22, 767– 779,

415   doi:10.1175/2008JCLI2641.1.

416 Liu, C., and E. J. Zipser (2015), The global distribution of largest, deepest, and most intense

417   precipitation systems, Geophys. Res. Lett., 42, 3591–3595.

418 Liu, C., D. J. Cecil, E. J. Zipser, K. Kronfeld, and R. E. Robertson (2012), Relationships

419   between lightning flash rates and radar reflectivity vertical structures in thunderstorms

420   over the tropics and subtropics, J. Geophys. Res., doi:10.1029/2011JD017123.

421   Liu, C., E. J. Zipser, and S. W. Nesbitt (2007), Global distribution of tropical deep

422   convection: Different perspectives from TRMM infrared and radar data, J. Clim., 20,

423   489–503.

424   Malkus, J. S., and H. Riehl (1964), Cloud structure and distributions over the tropical Pacific

425   Ocean, Tellus, 16, 275–287.

426   May, P. T., and A. P. Ballinger (2007), The statistical characteristics of convective cells in a

427   monsoon regime (Darwin, Northern Australia), Mon. Wea. Rev., 135, 82–92.

428   Nesbitt, S. W., E. J. Zipser, and D. J. Cecil (2000), A census of precipitation features in the

429   tropics using TRMM: Radar, ice scattering, and lightning observations, J. Clim., 13

430   (23), 4087–4106.

431   Nesbitt, S. W., R. Cifelli, and S. A. Rutledge (2006), Storm morphology and rainfall

432   characteristics of TRMM precipitation features, Mon. Wea. Rev., 134, 2702–2721.

433   Petersen, W. A., and S. A. Rutledge (2001), Regional Variability in Tropical Convection:

434   Observation from TRMM, J. Clim., 13, 4087–4106.

435   Qie, X. S., X. K. Wu, T. Yuan, J. C. Bian, and D. R. Lu (2014), Comprehensive Pattern of

436   Deep Convective Systems over the Tibetan Plateau–South Asian Monsoon Region

437   Based on TRMM Data, J. Clim., 27, 6612–6626, doi:10.1175/JCLI–D–14–00076.1.

438   Randel, W. J., M. Park Emmons, L. Kinnison, D. Bernath, P. Walker, K. Boone, and H.

439   Pumphrey (2010), Asian monsoon transport of pollution to the stratosphere, Science,

440   328, 611–613.

441   Riehl, H. and J. S. Malkus (1958), On the heat balance in the equatorial trough zone,

442   Geophysica, 6, 503-538.

443   Romatschke, U., and R. A. Houze Jr. (2013), Characteristics of precipitating convective

444   systems accounting for the summer rainfall of tropical and subtropical South America,

445   J. Hydrometeorol., 14, 25– 46.

446   Romatschke, U., and R. A. **Houze**, Jr. (2011), Characteristics of precipitating convective

447   systems in the South Asian monsoon, J. Hydrometeorol., **12**, 3-26.

448   Romatschke, U., S. Medina, and R. A. Houze Jr. (2010), Regional, seasonal, and diurnal

449   variations of extreme convection in the south Asian region, J. Clim., 23, 419–439.

450   Romatschke, U., S. Medina, and R. A. Houze Jr. (2010), Regional, seasonal, and diurnal

451   variations of extreme convection in the South Asian region, J. Clim., 23, 419– 439.

452   Sherwood, S. C. and A. E. Dessler (2000), On the control of stratospheric humidity, Geophys.

453   Res. Lett., 27, 2513–2516.

454   Subrahmanyam, K.V. and K. K. Kumar (2013), CloudSat observations of cloud-type

455   distribution over the Indian summer monsoon region, Ann. Geophys., 31, 1155-1162,

456   doi: 10.5194/angeo-31-1155-2013.

457   Subrahmanyam, K.V and K. K. Kumar (2018), Vertical structure of stratocumulus clouds and

458   associated dynamics over the Arabian Sea during Indian summer monsoon season, J.

459   Appl. Remote Sens. 12(1), 016018, doi: 10.1117/1.JRS.12.016018.

460   Subrahmanyam, K.V., K. K. Kumar and N. Reddy (2020), New insights into the convective

461   system characteristics over the Indian summer monsoon region using space based

462   passive and active remote sensing techniques, IETE Technical Review, 37:2, 211-

463   219, doi:10.1080/02564602.2019.1593890.

464   Tao, W.-K., et al. (2006), Retrieval of latent heating from TRMM measurements, Bull.

465   Amer. Meteorol. Soc., 87, 1555– 1572.

466   Toracinta, E. R., and E. J. Zipser (2001), Lightning and SSM/I-ice scattering mesoscale

467   convective systems in the global tropics, J. Appl. Meteorol., 40, 983–1002.

468   Uma, K. N., and T. N. Rao (2009), Characteristics of vertical velocity cores in different

469   convective systems observed over Gadanki, India, Mon. Weather Rev., 137, 954–975.

470   Wu, N., X. Zhuang, and Z. Meng (2020), Practical and Intrinsic Predictability of a Warm

471   Sector Torrential Rainfall Event in the South China Monsoon Region, J. Geophys.

472   Res., https://doi.org/10.1029/2019JD031313.

473   Wu, X., T. Yuan , R. Jiang, J. Li, Evolutionary Characteristics of Lightning and Radar Echo

474   Structure in Thunderstorms Based on the TRMM satellite, Atmos. Chem. Phys.

475   Discuss., https://doi.org/10.5194/acp-2018-778, 2018

476   Xu, W. (2011), East Asian summer monsoon precipitating systems: Rainfall characteristics,

477   storm morphologies and convective properties, Ph.D. dissertation, University of Utah,

478   pp. 293.

479   Xu, W., and E. J. Zipser (2012), Properties of deep convection in tropical continental,

480   monsoon, and oceanic rainfall regimes, Geophys. Res. Lett., 39, L07802, doi:10.1029/

481   2012GL051242.

482   Yuter, S. E., R. A. **Houze**, Jr., E. A. Smith, T. T. Wilheit, and E. Zipser (2005), Physical

483   characterization of tropical oceanic convection observed in KWAJEX, J. Appl.

484   Meteor., **44**, 385-415.

485   Zhag, C.-Z., Uyeda, H., H. Yamada, B. Geng and Y. Ni (2006), Characteristics of Mesoscale

486   Convective Systems over the East Part of Continental China during the Meiyu from

487   2001 to 2003, J. Meteor. Soci. of Japan, 84(4),763-782.

488 Zipser, E. J., D. J. Cecil, C. Liu, S. W. Nesbitt, and D. P. Yorty (2006), Where are the most

489   intense thunderstorms on earth?, Bull.Amer. Meteor. Soc., 87, 1057–1070.

490 Zuluaga, M. D., and R. A. Houze Jr. (2013), Evolution of the population of precipitating

491   convective systems over the Equatorial Indian Ocean in active phases of the

492   Madden-Julian Oscillation, J. Atmos. Sci., 70, 2713– 2725.

493